

## Continuous loading of a magneto-optical trap of Rb using a narrow transition

Rajnandan Choudhury Das , Thilagaraj Ravi , Samir Khan , and Kanhaiya Pandey \*

*Department of Physics, Indian Institute of Technology Guwahati, Guwahati, Assam 781039, India*

 (Received 18 January 2024; accepted 15 May 2024; published 10 June 2024)

We report continuous loading of  $^{87}\text{Rb}$  atoms in a magneto-optical trap (MOT) at narrow linewidth, 420-nm  $5S_{1/2}, F = 2 \rightarrow 6P_{3/2}, F = 3$  blue transition (blue MOT). Continuous loading of the blue MOT is achieved by superimposing the blue laser beam inside a hollow core of infrared (IR) laser beam driving the broad  $5S_{1/2}, F = 2 \rightarrow 5P_{3/2}, F = 3$  transition at 780 nm. We typically load  $\sim 10^8$  atoms in the blue MOT in 2.5 s. We characterize the continuous loading of the blue MOT with various parameters such as magnetic-field gradient, detuning, power and diameter of the blue MOT beam, and diameter of the hollow core (spot) inside the IR MOT beam. We observe that the blue laser beam should overflow the spot of the IR laser beam. This is because the blue laser cools the atoms to a lower temperature even in the presence of the broad IR laser, i.e., in the overlapped region, and hence helps in loading. To support the experimental result, we also present the theoretical framework for cooling atoms in the presence of two lasers driving two different transitions simultaneously. This method of continuous loading of the blue MOT can be useful to produce a continuous atomic beam of cold Rb atoms.

DOI: [10.1103/PhysRevA.109.063107](https://doi.org/10.1103/PhysRevA.109.063107)

### I. INTRODUCTION

Magneto-optical trapping (MOT) is the workhorse for all cold-atom experiments and is the basis of modern areas of research in quantum science and technology such as quantum computation and simulation, and quantum sensors. For MOT, the linewidth of the transition plays an important role. MOT at broader linewidth compared to narrow linewidth transition provides faster loading with higher capture velocity, but the final temperature happens to be higher. In order to achieve a higher number of atoms in MOT with low temperature, a two-step MOT is utilized [1–10]. In the first step, atoms are loaded in a MOT at a broad linewidth transition, and in the second step, atoms are transferred to the MOT at a narrow linewidth transition to achieve lower temperature, which means these two steps are separated in time. Instead of separating these two steps in time, one can also separate them in space, which results in the continuous loading of atoms in the MOT and is the key process for producing continuous Bose-Einstein condensate of Sr [11]. Continuous loading of the atoms in the MOT at narrow transition can enable us to generate a continuous beam of the cold atoms at lower temperatures, which offers a great advantage for atomic-based quantum sensors as it eliminates dead time.

The two-step MOT has been realized in Yb [1,2], Sr [3,11], Dy [4,5,12,13], Er [14–16], and Cd [17] (where the ratio of the linewidth of broad to narrow transition is in orders of magnitude) and also in alkali-metal elements [6–9,18] (where the ratio is 4–5 times). The continuous loading of the MOT at narrow transition precooled by broad transition has been realized for certain elements: Yb [1], Sr [11], and Dy [5]. In the case of Yb, continuous loading of the MOT at narrow transition

is superior in terms of the number of atoms and of course temperature [1,19,20]. The Yb MOT at broader transition has a lower number of atoms (even in the presence of repumper lasers [21]) as compared to the narrow transition. The MOT for alkali-metal atoms at narrow transitions in Li [6], K [7], and Rb [9,18,22] has been realized but continuous loading has not been reported yet. We use a core-shell MOT similar to that of the Yb [19], where a huge advantage was reported. In the scheme, a hole is created in the core of the laser beam driving the broad transition which is filled by the laser beam at a narrow transition. The relative dimension of the core and the filling beam is very important and depends upon the ratio of broad and narrow linewidth transitions. In the case of Yb, the ratio of the linewidth of broad to narrow transition is around 150 and the core should be just filled, as in the presence of the broad linewidth laser the weak transition laser (with intensity comparable to the saturation intensity) does not play a significant role in reducing the temperature. The case can be different in alkali-metal atoms where the linewidths of the broad and narrow transitions are only 4–5 times. In this case, the filling area should be bigger than the core area as in the overlapped region the narrow transition linewidth plays a role in reducing the temperature even in the presence of the broad transition.

In this paper, we present a method to load atoms continuously in the narrow-line MOT by superimposing the narrow-line beam inside the core of the broad transition beam. Using  $^{87}\text{Rb}$  atoms, we demonstrate the loading of  $1.2 \times 10^8$  atoms continuously in the blue MOT at 420 nm using the  $5S_{1/2}, F = 2 \rightarrow 6P_{3/2}, F = 3$  transition. We study the behavior of the blue MOT with various parameters such as magnetic-field gradient, detuning, power and diameter of the blue MOT beam, and diameter of the spot inside the infrared (IR) MOT beam.

The paper is organized as follows. In Sec. II, we describe the experimental setup. In Sec. III, we describe the theoretical

\*kanhaiyapandey@iitg.ac.in

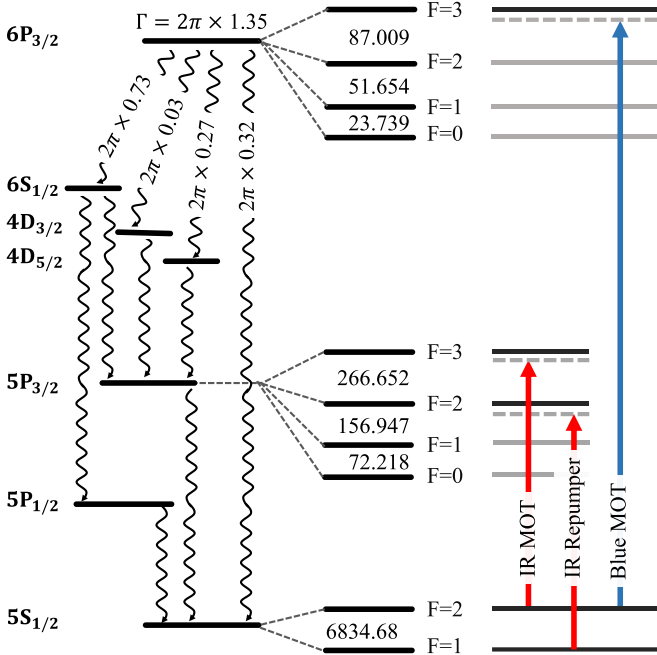


FIG. 1. The relevant energy levels of  $^{87}\text{Rb}$  with the hyperfine splitting and various decay paths of the  $6P_{3/2}$  state. Decay rates, the linewidth of the excited state, and the hyperfine splittings are shown in MHz. The figure is adapted from Ref. [9].

model for the calculation of force, diffusion, and temperature in the presence of the two transitions at 780 and 420 nm. In Sec. IV, we study the various effects due to magnetic-field gradient, detuning, power and diameter of the blue MOT laser, and diameter of the spot on the IR MOT laser. In Sec. V, we summarize our findings.

## II. EXPERIMENTAL SETUP

The relevant energy-level diagram and corresponding transitions utilized in this study are shown in Fig. 1. The laser system comprises one commercially (Toptica) available 420-nm (blue) external cavity diode laser (ECDL) and two home-assembled 780-nm (IR) ECDLs. The blue laser is divided into two parts: one for its frequency stabilization using saturation absorption spectroscopy (as described in Ref. [23]) and the second for cooling and trapping the atoms in the blue MOT. The probe beam in the spectroscopy setup is passed through one Rb vapor cell and detected on a high-speed and blue-color-sensitive photodetector (make: Thorlabs, model: APD430A2/M). The vapor cell is kept inside an oven at  $85^\circ\text{C}$ . The other part of the blue laser beam is sent through an acousto-optic modulator (AOM) in a double-pass configuration. It is up-shifted by around  $+2 \times 49.75$  MHz and is sent through the cell as a control beam with counterpropagating to the probe beam. This central frequency is adjusted to vary the detuning ( $\Delta_B$ ) of the blue MOT beam. The AOM frequency is modulated at 10 kHz to generate the error signal. Note that the probe beam is not modulated and thus gives a better signal-to-noise ratio than when it is modulated. The laser is locked corresponding to the  $5S_{1/2}$ ,  $F = 2 \rightarrow 6P_{3/2}$ ,  $F = 3$  peak. A portion of the leaked beam is used for monitoring the

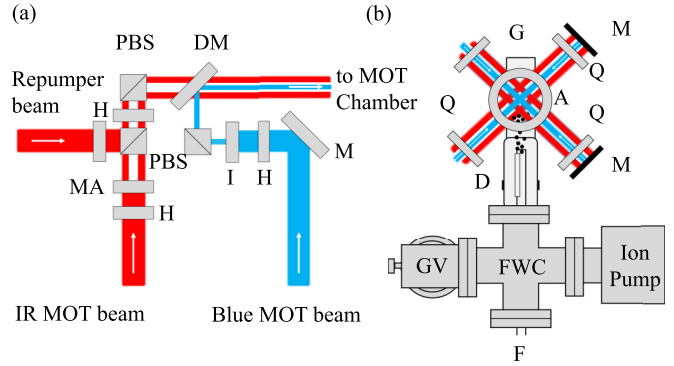


FIG. 2. (a) Mixing scheme of the three lasers. (b) Top view of the MOT setup. Figure abbreviations: A, anti-Helmholtz coil; D, Rb dispenser; DM, dichroic mirror; F, electric feedthrough; FWC, four-way cross; G, glass chamber; GV, all metal gate valve; H,  $\lambda/2$  wave-plate; I, iris; M, mirror; MA, mask; PBS, polarizing beam splitter; Q, dual  $\lambda/4$  wave-plate. The 780-nm and 420-nm beams are shown in red and blue, respectively.

single-mode operation and the wavelength of the 420-nm laser using a wavelength meter (make: Highfinesse GmbH, model: WS7-60).

The second part of the blue beam is passed through another AOM at  $+46.75$  MHz and its first-order beam is sent to the mixing scheme as shown in Fig. 2(a) after expanding it by 10 times. This AOM is used for switching the blue beam on and off and varying its power. An iris is used for changing the diameter of the blue beam ( $\phi_B$ ).

Polarization spectroscopy is employed for the two IR laser's frequency stabilization, as described in Ref. [9]. The IR MOT laser is locked to the  $5S_{1/2}$ ,  $F = 2 \rightarrow 5P_{3/2}$ ,  $F = (2, 3)$  crossover peak and the IR repumper laser is locked to the  $5S_{1/2}$ ,  $F = 1 \rightarrow 5P_{3/2}$ ,  $F = 1$  peak. Other parts of the IR MOT and repumper lasers are sent through two different AOMs at  $+123.5$  MHz and  $+150$  MHz, respectively, to address the  $5S_{1/2}$ ,  $F = 2 \rightarrow 5P_{3/2}$ ,  $F = 3$  and  $5S_{1/2}$ ,  $F = 1 \rightarrow 5P_{3/2}$ ,  $F = 2$  transitions. The first-order diffracted beams are then expanded 10 times individually and sent to the mixing scheme, as shown in Fig. 2(a).

On the path of the IR MOT beam, a circular mask (MA) is introduced so that a hollow core of diameter  $\phi_{\text{spot}}$  can be created inside the IR MOT beam. IR beams are then mixed on a polarizing beam splitter (PBS) and made the same polarized using another PBS and a half-plate. The vertical polarized beam from the PBS is mixed with the vertical polarized blue MOT beam using a dichroic mirror and made co-propagated, as shown in Fig. 2(a). The other two arms of the MOT beams with the same polarization are generated from the horizontally polarized beams from the PBS using two half wave-plates, two PBSs, and two dichroic mirrors (not shown in the schematics for simplification). All the beam's maximum diameter is limited to 16 mm due to the limitation set by the maximum diameter of the half wave-plates used in this experiment.

Three arms are then made circularly polarized using dual quarter wave-plates, sent to the rectangular glass MOT chamber, and retroreflected back using a combination of dual quarter wave-plates and mirrors [as shown in Fig. 2(b)].

The configuration of the MOT setup is the same as that in Ref. [9]. Atomic Rb vapors are introduced into the chamber by passing 2.15-A electric current to a dispenser (AlfaSource AS-Rb-0090-2C) inside the glass chamber.

The absorption imaging technique is used to capture the image of the atomic cloud on a CMOS camera (Thorlabs, CS135MUN) using an imaging beam. The imaging beam is 5 MHz red detuned from the  $5S_{1/2}$ ,  $F = 2 \rightarrow 5P_{3/2}$ ,  $F = 3$  transition. It is generated using a double-pass AOM and is coupled to a single-mode fiber. The camera's exposure time is 100  $\mu$ s, and the imaging beam is turned on for 52  $\mu$ s during the imaging cycle. The temperature of the cloud is determined from the time-of-flight method [18].

### III. THEORY

We have observed in the experiment (described in Sec. IV) that the size of the blue MOT beam should be bigger than the size of the hollow core (spot) in the IR MOT beam for loading a higher number of atoms. This implies that there is an overlapped region for the two lasers and hence both transitions are driven simultaneously in this region. In order to analyze the cooling mechanism in the presence of both transitions, we use the density matrix approach in one dimension. We consider that two (counterpropagating) laser beams are driving the transition  $|1\rangle$  ( $5S_{1/2}$ ,  $F = 2$ )  $\rightarrow$   $|2\rangle$  ( $5P_{3/2}$ ,  $F = 3$ ) at 780 nm and two (counterpropagating) laser beams are driving the transition  $|1\rangle$  ( $5S_{1/2}$ ,  $F = 2$ )  $\rightarrow$   $|3\rangle$  ( $6P_{3/2}$ ,  $F = 3$ ) at 420 nm.

The Hamiltonian ( $H$ ) for the three-level system can be written as

$$H = -\hbar\delta_{12}^+|2\rangle\langle 2| - \hbar\delta_{13}^+|3\rangle\langle 3| + \left[ \left\{ \frac{\hbar\Omega_{12}^+}{2} + \frac{\hbar\Omega_{12}^-}{2} e^{i(\delta_{12}^+ - \delta_{12}^-)t} \right\} |1\rangle\langle 2| + \left\{ \frac{\hbar\Omega_{13}^+}{2} + \frac{\hbar\Omega_{13}^-}{2} e^{i(\delta_{13}^+ - \delta_{13}^-)t} \right\} |1\rangle\langle 3| + \text{H.c.} \right]. \quad (1)$$

Here  $\delta_{12}^{+(-)}$  and  $\delta_{13}^{+(-)}$  are the detuning of the 780- and 420-nm laser beams propagating in the positive (negative) direction, respectively. For the atoms moving in the positive direction with velocity  $v$ ,  $\delta_{12}^+ = \delta_{12} - k_{12}v$ ,  $\delta_{13}^+ = \delta_{13} - k_{13}v$ ,  $\delta_{12}^- = \delta_{12} + k_{12}v$ , and  $\delta_{13}^- = \delta_{13} + k_{13}v$ . Here,  $k_{12} = 2\pi/780$  nm and  $k_{13} = 2\pi/420$  nm, and  $\delta_{12}$  and  $\delta_{13}$  are detuning of the 780- and 420-nm lasers for stationary atoms.  $\Omega_{12}^+ = \Omega_{12}^- = \Omega_{12}$  and  $\Omega_{13}^+ = \Omega_{13}^- = \Omega_{13}$  are the Rabi frequencies of the 780- and 420-nm lasers.

The atom-field interaction is described by writing the Liouville–von Neumann equation for the density matrix [24] as follows:

$$\frac{d\rho}{dt} = -\frac{i}{\hbar}[H, \rho] + L(\rho), \quad (2)$$

where  $\rho$  is the density matrix and  $L(\rho)$  accounts for the spontaneous decay. The equations of motion of the density matrix are obtained by solving Eqs. (1) and (2). Since the Hamiltonian has harmonically oscillating terms at two different frequencies, Floquet expansion for the density matrix

elements is used as follows (similar to Refs. [24,25]),

$$\rho_{ij}(t) = \sum_{m=-\infty}^{\infty} \sum_{n=-\infty}^{\infty} \rho_{ij}^{(m,n)}(t) e^{i(m\Delta_1 + n\Delta_2)t}, \quad (3)$$

where  $\Delta_{1(2)} = -2k_{12(13)}v$ . The Floquet expansion is truncated up to second order and substituted in the density matrix equations, and coefficients of the same power in  $(m\Delta_1, n\Delta_2)$  are compared to obtain the simultaneous differential equations and then numerically solved to find all the coefficients.

The absorptions of the 780-nm laser beam propagating in positive and negative directions are given by  $\text{Im}(\rho_{12}^{(0,0)})$  and  $\text{Im}(\rho_{12}^{(1,0)})$ , respectively, and similarly for the blue beams the absorptions are given by  $\text{Im}(\rho_{13}^{(0,0)})$  and  $\text{Im}(\rho_{13}^{(0,1)})$ . All other coefficients denote the wave mixing. Here  $\text{Im}\{\cdot\}$  denotes the imaginary part. The damping force on the atoms in the presence of the two lasers can be given as

$$F_{\text{damp}} = \hbar[k_{12}\Omega_{12} \text{Im}(\rho_{12}^{(0,0)} - \rho_{12}^{(1,0)}) + k_{13}\Omega_{13} \text{Im}(\rho_{13}^{(0,0)} - \rho_{13}^{(0,1)})]. \quad (4)$$

The force,  $F_{\text{damp}}/(\hbar k_{12}\Gamma_{12})$ , vs velocity,  $k_{12}v/\Gamma_{12}$ , is plotted in Fig. 3(a). The parameters used for this plot are  $\delta_{12}/\Gamma_{12} = \delta_{13}/\Gamma_{13} = -1/2$  and  $I/I_s = 1/10$  for both the lasers. Here,  $\Gamma_{12(13)}$  is the linewidth of the 780- (420-) nm transition and  $I_s$  is the saturation intensity. The red dashed (blue dotted) line corresponds to the force in the presence of only the 780- (420-) nm laser. The black solid line represents the net force in the presence of both lasers. For very low velocity,  $F_{\text{damp}} = -\beta v$ , where  $\beta$  is known as the damping coefficient. From Fig. 3(a), it is clear that  $\beta_{420} > \beta_{780}$  and  $\beta_{420} \approx \beta_{\text{both}}$ , where  $\beta_{780(420)}$  is the  $\beta$  in the presence of only the 780- (420-) nm laser and  $\beta_{\text{both}}$  is the  $\beta$  in the presence of both the lasers. This implies that once the atoms are cooled by the IR laser in the outer region and enter into the overlapped region of the IR and blue lasers, then the atoms are further cooled down dominantly by the blue laser.

The diffusion coefficient in the presence of both the driving lasers can be given as

$$D = \hbar^2[k_{12}^2\Omega_{12} \text{Im}(\rho_{12}^{(0,0)} + \rho_{12}^{(1,0)}) + k_{13}^2\Omega_{13} \text{Im}(\rho_{13}^{(0,0)} + \rho_{13}^{(0,1)})]. \quad (5)$$

The diffusion coefficient,  $D/(\hbar k_{12})^2\Gamma_{12}$ , vs velocity,  $k_{12}v/\Gamma_{12}$ , plot is shown in Fig. 3(b) for the same parameters as in Fig. 3(a). Two-dimensional color plot of force vs position and velocity for two spot sizes of 3 mm and 9 mm at  $\phi_B = 16$  mm,  $\Omega_{12} = \Gamma_{12}/\sqrt{2}$ ,  $\Omega_{13} = \Gamma_{13}/\sqrt{2}$ ,  $\delta_{12} = -10$  MHz, and  $\delta_{13} = -7$  MHz are shown in Figs. 3(c) and 3(d), respectively. The IR transition has a stronger damping force as compared to the blue transition. The larger spot size reduces the region/area of the stronger damping force and hence reduces the number of atoms in the blue MOT.

Then the effective temperature is found using the Einstein relation,  $T = D(0)/\beta k_B$ , where  $D(0)$  is the diffusion coefficient at zero velocity and  $k_B$  is the Boltzmann constant [26]. The temperature vs intensity of the 420-nm laser ( $I_{420}$ ) is plotted in Fig. 4 for various intensities of the 780-nm laser ( $I_{780}$ ) at  $\delta_{12}/\Gamma_{12} = \delta_{13}/\Gamma_{13} = -1/2$ . In the absence of the 780-nm laser (dark blue line at the bottom),  $T$  decreases

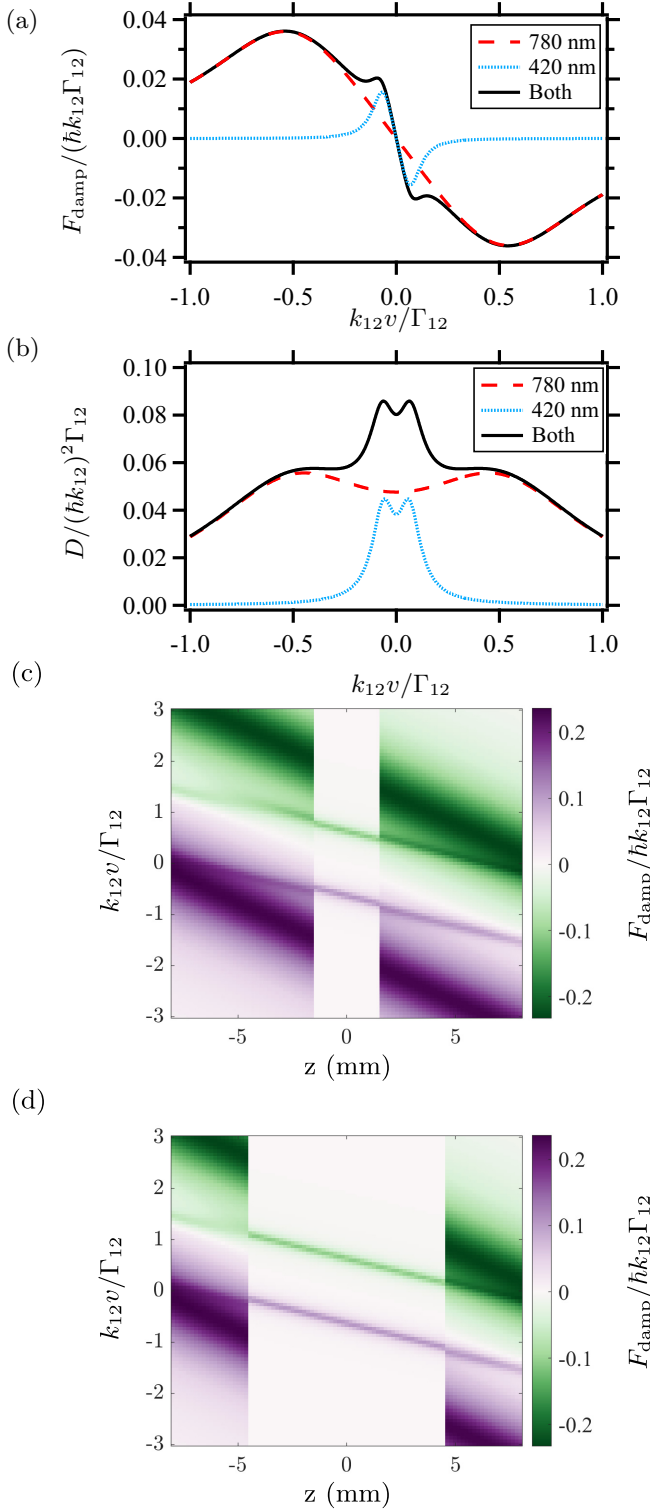


FIG. 3. (a) Force,  $F$ , and (b) diffusion coefficient,  $D$ , vs velocity plot at  $\delta_{12}/\Gamma_{12} = \delta_{13}/\Gamma_{13} = -1/2$  and  $I/I_s = 1/10$  for both the lasers. The red dashed line, the blue dotted line, and the black solid line correspond to  $F$  [in panel (a)] and  $D$  [in panel (b)] in the presence of only the 780-nm laser, only the 420-nm laser, and both lasers, respectively. Two-dimensional color plot of force vs position and velocity for two spot sizes of (c) 3 mm and (d) 9 mm at  $\phi_B = 16$  mm,  $\Omega_{12} = \Gamma_{12}/\sqrt{2}$ ,  $\Omega_{13} = \Gamma_{13}/\sqrt{2}$ ,  $\delta_{12} = -10$  MHz, and  $\delta_{13} = -7$  MHz.  $k_{12}$  is the magnitude of the wave vector of the 780-nm laser and  $\Gamma_{12}$  is the linewidth of the IR transition.

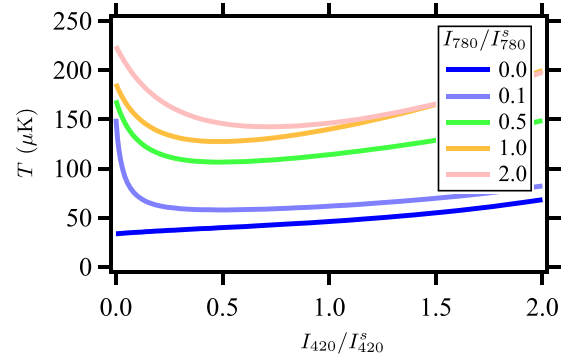


FIG. 4. Temperature vs intensity of the 420-nm laser at various intensities of the 780-nm laser.

linearly with the decrease in  $I_{420}$  and reaches the Doppler temperature ( $T_D$ ) corresponding to the blue transition, given by  $\hbar\Gamma_{13}/2k_B = 34 \mu\text{K}$ . Note that  $T_D$  at 780 nm is  $\sim 150 \mu\text{K}$ . As the intensity of the IR laser increases in the absence of the blue laser, the  $T$  also increases. However,  $T$  decreases in the presence of the 420-nm laser, as shown by the light blue (dark gray) curve in Fig. 4. For fixed IR laser intensity,  $T$  initially decreases with an increase in  $I_{420}$ , reaches a minimum, and then increases with a further increase in  $I_{420}$ . We also observe experimentally that the temperature of the IR MOT decreases from  $\sim 1$  mK (in the absence of the blue laser) to  $\sim 400 \mu\text{K}$  (in the presence of the blue laser at  $\Delta_B = -3$  MHz). Thus, in the overlapped region, the laser driving the narrow linewidth transition further reduces the speed of the atoms (than the outer region) before it reaches the core region where only the laser driving the narrow linewidth transition is present. This suggests that the overlapped region in the broad and narrow linewidth transitions affects the continuous loading of the atoms in the narrow-line MOT and eventually the number of atoms in the blue MOT.

Note that for low intensities (in comparison to saturation intensities) of 780- and 420-nm laser beams, the V systems behave as two separate two-level systems ( $|1\rangle \rightarrow |2\rangle$  and  $|1\rangle \rightarrow |3\rangle$ ). The  $T$  for very low intensity of the 780- and 420-nm lasers is given as

$$T_D = \frac{\hbar}{2k_B} \frac{\Gamma_{12}s_{12}k_{12}^2 + \Gamma_{13}s_{13}k_{13}^2}{s_{12}k_{12}^2 + s_{13}k_{13}^2}. \quad (6)$$

Here,  $s_{12(13)}$  is the saturation parameter of the 780- (420-) nm laser.

#### IV. RESULTS AND DISCUSSION

Initially, the diameter of all the beams is kept at a maximum, i.e., 16 mm. The diameter of the spot introduced in the core of the IR MOT beam is  $\phi_{\text{spot}} = 6$  mm and superimposed with the blue beam. The total power of the IR MOT, repumper, and blue MOT beams is 50 mW, 13 mW, and 25 mW, respectively. Detuning of the respective lasers is  $-10$  MHz,  $-7$  MHz, and  $-7$  MHz, respectively. A magnetic-field gradient ( $B'$ ) of 12.6 G/cm is produced using an anti-Helmholtz coil. We observe that the number of atoms in the blue MOT ( $N$ ) saturates to  $1.2 \times 10^8$ , and its loading time is 2.5 s.

We study the effect of detuning of the blue laser ( $\Delta_B$ ) on  $N$  at three different magnetic-field gradients. The blue laser's

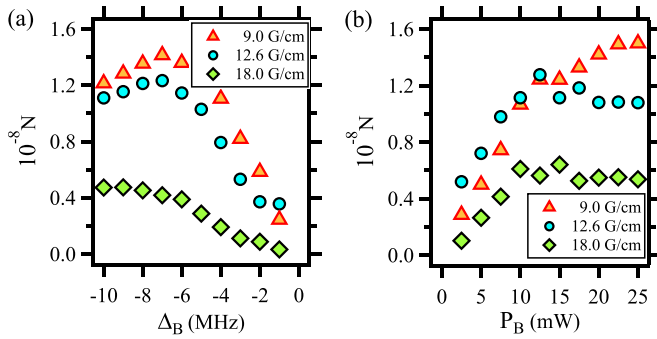


FIG. 5. Number of atoms ( $N$ ) vs (a) detuning ( $\Delta_B$ ) and (b) power ( $P_B$ ) of the blue laser at three different magnetic-field gradients: 9 G/cm (orange triangle), 12.6 G/cm (blue circle), and 18 G/cm (green diamond). In panel (a),  $P_B = 25$  mW. In panel (b),  $\Delta_B = -7$  MHz. In panels (a) and (b),  $\phi_B = 16$  mm and  $\phi_{\text{spot}} = 6$  mm.

power ( $P_B$ ) is 25 mW. As shown in Fig. 5(a),  $N$  increases slightly to  $1.2 \times 10^8$  at 12.6 G/cm when  $\Delta_B$  is changed from  $-10$  MHz to  $-7$  MHz. When  $\Delta_B$  is further varied towards resonance,  $N$  decreases, and the MOT disappears. When the magnetic-field gradient is increased (decreased) to 18 G/cm (9 G/cm),  $N$  decreases (increases).

Next, we vary the power of the blue laser ( $P_B$ ) at  $\Delta_B = -7$  MHz (i.e.,  $\Delta_B = -5\Gamma_{13}$ ) and study its effect on  $N$  at three different magnetic-field gradients, as shown in Fig. 5(b). At 18 G/cm (green diamond), with the increase in  $P_B$  from 2.5 to 10 mW,  $N$  increases to  $6 \times 10^7$  and saturates with further increase in  $P_B$ . Similar trends are observed for 12.6 G/cm (blue circle) and 9 G/cm (orange triangle). However,  $P_B$  for  $N$  to reach saturation increases with an increase in magnetic-field gradients.

We then switch off the IR MOT beam and optimize the blue MOT beam to decrease its temperature by lowering its power to 5 mW and changing its detuning to  $-3$  MHz. After a hold time of 20 ms, the blue MOT beam and the magnetic field are switched off. We measure the temperature of the blue MOT to be around  $\sim 90$   $\mu$ K.

To study the effect of the diameter of the blue beam ( $\phi_B$ ), we measure  $N$  at different  $\phi_B$ . Figure 6(a) shows the  $N$  vs  $\phi_B$  data for the 6-mm diameter of the spot ( $\phi_{\text{spot}}$ ). We observe that, with an increase in  $\phi_B$  from 4 mm to 8 mm,  $N$  increases

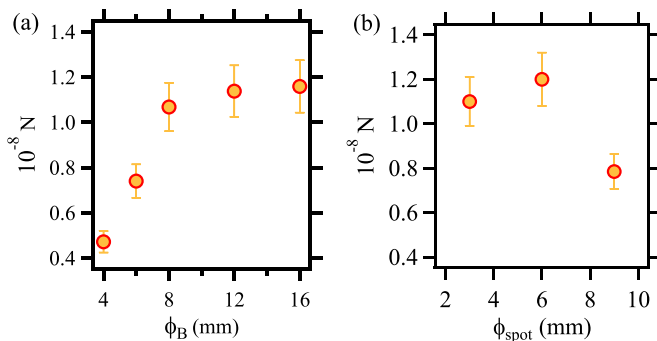


FIG. 6. Number of atoms ( $N$ ) in the blue MOT vs diameter of the (a) blue beam ( $\phi_B$ ) and (b) spot ( $\phi_{\text{spot}}$ ). In panel (a),  $\phi_{\text{spot}} = 6$  mm. In panel (b),  $\phi_B = 16$  mm.

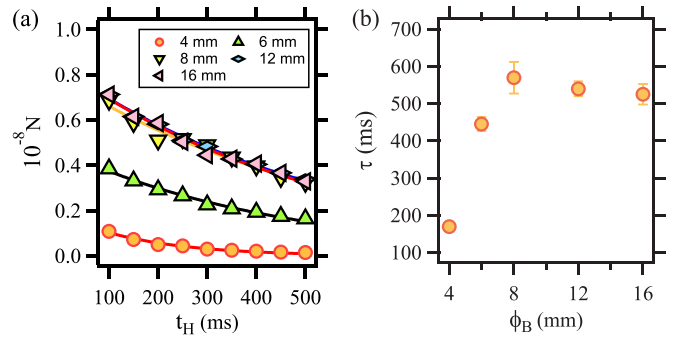


FIG. 7. (a) Number of atoms ( $N$ ) in the blue MOT vs hold time ( $t_H$ ) for different diameters of the blue beam. The solid lines in panel (a) are exponential fits to the  $N$  vs  $t_H$  data. (b) Lifetime ( $\tau$ ) of the blue MOT vs diameter of the blue beam ( $\phi_B$ ). In panels (a) and (b),  $\phi_{\text{spot}} = 6$  mm and  $B' = 12.6$  G/cm.

from  $4.5 \times 10^7$  to  $1.1 \times 10^8$ . With further increases in  $\phi_B$ , there is no significant improvement in  $N$ . A similar trend is observed for the spot size of 3 mm. We observe that for better loading of the continuous blue MOT, the diameter of the blue beam should be bigger than the diameter of the spot.

Next, we study  $N$  at three different diameters of the spot. Figure 6(b) shows the variation of the  $N$  vs  $\phi_{\text{spot}}$  data for the 16-mm diameter of the blue beam ( $\phi_B$ ). When  $\phi_{\text{spot}}$  is increased from 3 mm to 6 mm, we observe a slight increase in the number of atoms in the blue MOT to  $N = 1.2 \times 10^8$ . With a further increase in  $\phi_{\text{spot}}$  to 9 mm,  $N$  significantly drops to  $8 \times 10^7$ . Although  $N$  corresponding to  $\phi_{\text{spot}} = 3$  mm is slightly lower than that with  $\phi_{\text{spot}} = 6$  mm, the lifetime of the blue MOT with  $\phi_{\text{spot}} = 3$  mm is around 3 times lower than the lifetime with  $\phi_{\text{spot}} = 6$  mm. The number of atoms in the MOT is decided by the loading rate and loss rate (lifetime). The IR transition has a stronger damping force as compared to the blue transition. The larger spot size reduces the region/area of stronger damping force [as shown in Figs. 3(c) and 3(d)] and hence reduces the number of atoms in the blue MOT. Smaller spot size increases the stronger trapping region but reduces the lifetime of the blue MOT and hence there is a slight decrease in the number of atoms in the blue MOT as shown in Fig. 6(b).

We further study the effect of the diameter of the blue beam ( $\phi_B$ ) on the lifetime ( $\tau$ ) of the blue MOT. First, we measure  $N$  at different hold times ( $t_H$ ) of the blue MOT and fit the  $N$  vs  $t_H$  data with the following equation:  $N = N_0 \times \exp(-t_H/\tau)$ . Figure 7(a) shows the variation of  $N$  with  $t_H$  at different  $\phi_B$  for the blue MOT with a spot size of 6 mm. The solid lines in Fig. 7(a) are exponential fits to the  $N$  vs  $t_H$  data. Figure 7(b) shows the corresponding lifetime ( $\tau$ ) with  $\phi_B$ . We observe that when  $\phi_B$  is 4 mm, the lifetime of the blue MOT is around 180 ms. It increases to 550 ms when  $\phi_B$  is increased to 8 mm and then remains the same even after increasing  $\phi_B$  to 16 mm.

## V. CONCLUSIONS

In summary, we have demonstrated the continuous loading of  $^{87}\text{Rb}$  atoms in the blue MOT with a typical number of  $1.2 \times 10^8$  atoms in 2.5 s. The continuous loading of the blue MOT is achieved by superimposing the blue laser beam inside

the hollow core (spot) of the IR laser beam driving the broad transition. In order to achieve maximum loading, the spot size should be 6 mm for the total diameter of 16 mm for the IR laser beam and the size of the blue laser beam should be more than 6 mm. This means that the blue laser beam should overflow the spot of the IR laser beam. We have also measured the lifetime of the blue MOT with various diameters of the blue laser beam and found around 500 ms for a beam diameter of more than 6 mm. Although we do not see an increased number of atoms in the continuously loaded blue MOT in comparison to the IR MOT (in contrast to the Yb core-shell

MOT experiment [19]), this method of continuous loading of the blue MOT can be useful to produce continuous atomic beams of cold Rb atoms.

#### ACKNOWLEDGMENTS

R.C.D. would like to acknowledge the Ministry of Education, Government of India, for the Prime Minister's Research Fellowship (PMRF). K.P. would like to acknowledge the funding from DST through Grant No. DST/ICPS/QuST/Theme-3/2019.

- 
- [1] T. Kuwamoto, K. Honda, Y. Takahashi, and T. Yabuzaki, Magneto-optical trapping of Yb atoms using an intercombination transition, *Phys. Rev. A* **60**, R745(R) (1999).
- [2] K. Pandey, K. D. Rathod, A. K. Singh, and V. Natarajan, Atomic fountain of laser-cooled Yb atoms for precision measurements, *Phys. Rev. A* **82**, 043429 (2010).
- [3] T. Yang, K. Pandey, M. S. Pramod, F. Leroux, C. C. Kwong, E. Hajiyevev, Z. Y. Chia, B. Fang, and D. Wilkowski, A high flux source of cold strontium atoms, *Eur. Phys. J. D* **69**, 226 (2015).
- [4] M. Lu, S. H. Youn, and B. L. Lev, Spectroscopy of a narrow-line laser-cooling transition in atomic dysprosium, *Phys. Rev. A* **83**, 012510 (2011).
- [5] T. Maier, H. Kadau, M. Schmitt, A. Griesmaier, and T. Pfau, Narrow-line magneto-optical trap for dysprosium atoms, *Opt. Lett.* **39**, 3138 (2014).
- [6] P. M. Duarte, R. A. Hart, J. M. Hitchcock, T. A. Corcovilos, T.-L. Yang, A. Reed, and R. G. Hulet, All-optical production of a lithium quantum gas using narrow-line laser cooling, *Phys. Rev. A* **84**, 061406(R) (2011).
- [7] D. C. McKay, D. Jervis, D. J. Fine, J. W. Simpson-Porco, G. J. A. Edge, and J. H. Thywissen, Low-temperature high-density magneto-optical trapping of potassium using the open  $4s \rightarrow 5p$  transition at 405 nm, *Phys. Rev. A* **84**, 063420 (2011).
- [8] J. Sebastian, C. Gross, K. Li, H. C. J. Gan, W. Li, and K. Dieckmann, Two-stage magneto-optical trapping and narrow-line cooling of  $^6\text{Li}$  atoms to high phase-space density, *Phys. Rev. A* **90**, 033417 (2014).
- [9] R. C. Das, D. Shylla, A. Bera, and K. Pandey, Narrow-line cooling of  $^{87}\text{Rb}$  using  $5S_{1/2} \rightarrow 6P_{3/2}$  open transition at 420 nm, *J. Phys. B: At. Mol. Opt. Phys.* **56**, 025301 (2023).
- [10] Y. Miyazawa, R. Inoue, H. Matsui, K. Takanashi, and M. Kozuma, Narrow-line magneto-optical trap for europium, *Phys. Rev. A* **103**, 053122 (2021).
- [11] C.-C. Chen, R. González Escudero, J. Minář, B. Pasquiou, S. Bennetts, and F. Schreck, Continuous Bose-Einstein condensation, *Nature (London)* **606**, 683 (2022).
- [12] M. Lu, S. H. Youn, and B. L. Lev, Trapping ultracold dysprosium: A highly magnetic gas for dipolar physics, *Phys. Rev. Lett.* **104**, 063001 (2010).
- [13] M. Lu, N. Q. Burdick, S. H. Youn, and B. L. Lev, Strongly dipolar Bose-Einstein condensate of dysprosium, *Phys. Rev. Lett.* **107**, 190401 (2011).
- [14] A. J. Berglund, J. L. Hanssen, and J. J. McClelland, Narrow-line magneto-optical cooling and trapping of strongly magnetic atoms, *Phys. Rev. Lett.* **100**, 113002 (2008).
- [15] A. Frisch, K. Aikawa, M. Mark, A. Rietzler, J. Schindler, E. Zupanič, R. Grimm, and F. Ferlaino, Narrow-line magneto-optical trap for erbium, *Phys. Rev. A* **85**, 051401(R) (2012).
- [16] B. Seo, P. Chen, Z. Chen, W. Yuan, M. Huang, S. Du, and G.-B. Jo, Efficient production of a narrow-line erbium magneto-optical trap with two-stage slowing, *Phys. Rev. A* **102**, 013319 (2020).
- [17] A. Yamaguchi, M. S. Safronova, K. Gibble, and H. Katori, Narrow-line cooling and determination of the magic wavelength of Cd, *Phys. Rev. Lett.* **123**, 113201 (2019).
- [18] R. Ding, A. Orozco, J. Lee, and N. Claussen, [Narrow-linewidth laser cooling for rapid production of low-temperature atoms for high data-rate quantum sensing](#), Technical Report, US Department of Energy, LDRD Project No. 226345, November 2022.
- [19] J. Lee, J. H. Lee, J. Noh, and J. Mun, Core-shell magneto-optical trap for alkaline-earth-metal-like atoms, *Phys. Rev. A* **91**, 053405 (2015).
- [20] B. Plotkin-Swing, A. Wirth, D. Gochnauer, T. Rahman, K. E. McAlpine, and S. Gupta, Crossed-beam slowing to enhance narrow-line ytterbium magneto-optic traps, *Rev. Sci. Instrum.* **91**, 093201 (2020).
- [21] J. W. Cho, H.-G. Lee, S. Lee, J. Ahn, W.-K. Lee, D.-H. Yu, S. K. Lee, and C. Y. Park, Optical repumping of triplet- $p$  states enhances magneto-optical trapping of ytterbium atoms, *Phys. Rev. A* **85**, 035401 (2012).
- [22] R. C. Das, S. Khan, T. R., and K. Pandey, Role of spontaneously generated coherence (SGC) in laser cooling of atoms, [arXiv:2402.04234](#).
- [23] R. C. Das, S. Khan, T. Ravi, and K. Pandey, Direct spectroscopy of rubidium using a narrow-line transition at 420 nm, *Eur. Phys. J. D* **78**, 40 (2024).
- [24] E. O. Nyakang'o and K. Pandey, Resolving closely spaced levels for Doppler mismatched double resonance, *Phys. Rev. A* **103**, 013107 (2021).
- [25] E. O. Nyakang'o and K. Pandey, Role of velocity induced coherent population oscillation in saturated fluorescence spectroscopy, *Eur. Phys. J. D* **74**, 1434 (2020).
- [26] S. Chang and V. Minogin, Density-matrix approach to dynamics of multilevel atoms in laser fields, *Phys. Rep.* **365**, 65 (2002).